Photoacoustic simulation of microvessel bleeding: Spectral analysis and its implication for monitoring vascular-targeted treatments

Muhannad N. Fadhel[1,2], Eno Hysi[1,2], Jason Zalev[1,2,3], Michael C. Kolios[1,2*]

[1] Ryerson University, Department of Physics, Toronto, Canada
[2]Institute for Biomedical Engineering, Science and Technology, Keenan Research Center, St. Michael's Hospital, Toronto, Canada
[3]Seno Medical Instruments, San Antonio, TX, USA
*mkolios@ryerson.ca

ABSTRACT

The destruction of blood vessels is a commonly used cancer therapeutic strategy. Bleeding consequently follows and leads to the accumulation of blood in the interstitium. Photoacoustic (PA) imaging is well positioned to detect bleeding due to its sensitivity to hemoglobin. After treatment vascular disruption can occur within just a few hours, which leads to bleeding which might be detected using PA to assess therapeutic effectiveness. Deep microvessels cannot typically be resolved using acoustic-resolution PA. However, spectral analysis of PA signals may still permit assessment of bleeding. This paper introduces a theoretical model to simulate the PA signals from disrupted vessels using a fractal model. The fractal model uses bifurcated-cylinder bases to represent vascular trees. Vessels have circular absorption cross-sections. To mimic bleeding from blood vessels, the diffusion of hemoglobin from microvessels was simulated. The PA signals were computed and in the simulations were detected using a linear array transducer (30 MHz center frequency) for four different vascular trees (at 256 axial spatial locations/tree). The Fourier Transform of each beamformed PA signal was computed and the power spectra were fitted to a straight line within the -6 dB bandwidth of the receiving transducer. When comparing the power spectra before and after simulated bleeding, the spectral slope and midband fit (MBF) parameters decreased by 0.12 dB/MHz and 2.12 dB, while the y-intercept did not change after 1 hour of simulated bleeding. The results suggest that spectral PA analysis is sensitive to changes in the concentration and spatial distribution of hemoglobin in tissue, and changes due to bleeding can be detected without the need to resolve individual vessels. The simulations support the applicability of PA imaging in cancer treatment monitoring by detecting microvessel disruption.

Keywords: vascular tree model, photoacoustics modeling, spectral analysis, cancer treatment monitoring.

1. INTRODUCTION

Photoacoustic (PA) imaging has been proposed to monitor tumour response to various types of cancer therapies [1], [2]. A common response to these therapies can involve bleeding of tumour microvessels. The ability to detect and quantify the occurrence of bleeding can have an important role for PA in cancer therapy.

One of such emerging treatments involves ultrasound activated microbubbles [3]. The microbubbles target microvessels resulting in the escape of hemoglobin to the surrounding tissues [4], [5]. Microbubble shell disruption induces damage to the endothelial cells lining the vessels. The outcome is vessel disruption followed by tumour cell death and extensive haemorrhagic necrosis within hours of treatment delivery [4], [6]. Coupling microbubbles with radiation therapy has been shown to create a synergistic effect to induce tumour cell death.

PA imaging is a non-invasive modality for imaging deep into the tissues (> 1 cm) at high resolutions of less than 200 μm. Most studies in PA imaging focuses on analyzing the amplitude of the generated PA signal [7]. However, deep microvessels cannot typically be resolved using acoustic-resolution PA. Nevertheless, spectral analysis of the PA signals may still permit assessment of bleeding through the spectral analysis of the PA signals. Spectral analysis can involve both optical spectral analysis (for the identification of chromophores), and spectral analysis of the photoacoustically generated ultrasound signals detected. This paper focuses on the later.

The potential of spectral analysis of PA signals has not been fully investigated, especially for cancer treatment monitoring. Utilizing spectral analysis can improve the sensitivity of PA imaging in detecting changes on scales that cannot be spatially resolved, due to the changes in the frequency content of the PA signals generated that are the result of changes in the size and spatial distribution of that dominant optical absorbing structures. This is analogous to how such techniques are used in quantitative ultrasound [8], [9].

PA spectral analysis is used to acquire system independent information about the optically absorbing source [10], [11]. The information can be correlated to the size and concentration of the optical absorbers in the tissue, which are dominated by the red blood cells in the blood. In order to extract spectral parameters, the time-domain PA signals are transformed to the frequency-domain. The system dependencies are removed from the PA power spectra using a reference power spectrum. The slope, y-intercept and midband fit (MBF) parameters are extracted from the line of best fit and are correlated to microstructures in the tissues. The advantages of PA spectral analysis have been demonstrated in assessing tumours, liver conditions and osteoporotic patients [12]–[17].

Simulations of vascular disruption resulting in hemorrhaging were performed, as described in this paper. To our knowledge, such analysis has not been done before. To simulate bleeding from tumour vessels, modelling of a tumour vasculature was performed using a vascular tree model. The bases of the model are composed of cylinders which bifurcate into two daughter vessels [18]–[22]. The length, diameter and branching angle of the daughter vessels is controlled by selecting different parameters as shown in Figure 1 (a). These parameters can be altered to represent different vessel structures within the body. Modeling bleeding as a result of microbubble collapse can be achieved by using Fick's law of diffusion, as it has been used in modeling the extravasation of blood outside the vessels [23]–[25]. These simulations can provide an insight into the potential of using PA spectral analysis used to assess the efficacy of cancer therapy. This could potentially improve outcome and reduce the reoccurrence rate of tumours by providing timely feedback on the effectiveness of the drug / therapeutic approach.

2. METHODOLOGY

The vascular tree structure of tumour vessels was simulated using a fractal model with a cylindrical basis [18]–[22]. The extravasation of blood outside the vessels due to microbubble collapse was simulated using Fick's law of diffusion, as it has been used to model bleeding [23]–[25]. The PA signals of an omni-directional point detector were generated from the solution to the PA wave equation using a Green's function approach. The directivity and sensitivity to detector specific frequencies was accounted for. The simulated signals were used to generate 2D PA images using a delay-and-sum beamforming approach. Spectral analysis was performed by extracting the spectral slope, MBF and y-intercept, as described elsewhere [9].

2.1. Vascular tree modeling

The vascular tree to represent tumour vessels is generated using a fractal model. In this paper, the parameters were selected to model chaotic vessels similar to vessels found in tumours (Figure 1 (a)). The simulations were performed in three dimensions. The third branch with a diameter of 150 μm and length of 1 mm was simulated at the origin,

leading up to the 12th branch with a diameter of approximately 14 μm and a length of 0.35 mm. These values were chosen to mimic measured tumour vasculatures of mammary carcinoma [26].

The size of the daughter fragments is determined by the bifurcation index (β). The bifurcation index is used to correlate the left and right daughter segment through the equation below:

$$\beta = D_R / D_L$$
<div align="right">*Equation 1*</div>

where the β value ranges between $0 < \beta < 1$. The left daughter segment (D_L) is assumed to be larger than right daughter segment (D_R) to represent the diameter asymmetry. Solving for D_L and D_R can be achieved using the hemodynamic energy minimizing constrains. β was fixed to a value of 0.95 for this simulation. The distance factor is used (k) is used to correlate the length (L) of the daughter and parent segments. The distance factor usually has a values from 0.7 to 0.9 and is set to 0.9 for this simulation. The last parameter controls the branching angle of the daughter segments with respect to the parent segment. Since the simulations are done in 3D, there are two angles for each daughter segment. The first angle is called the branching orientation (φ) and ranges from 0° to 360° while the other angle is called the branching angle (θ) and ranges from 25° to 140°. These values are used to simulate chaotic vasculature to represent tumour vessels [18], [19].

2.2. PA signal generation

When short laser pulses irradiate optically absorbing objects, the absorbers emit PA waves that carry their geometric information. The PA signal can be computed for a defined laser profile $I(r, t)$ and the absorption coefficient map of the tissue $\mu_a(r, t)$. The product of these two parameters results in the heating function $H(r, t)$. The heating function was used to compute the shape of the generated PA signal. The forward solution of the PA wave equation was computed based on the free-space Green's function:

$$p(r,t) = \frac{B}{4\pi C_p} \iiint \left| \frac{d^3 r' \delta H(r',t)}{|r-r'|\delta t'} \right|_{t'=t-\frac{|r-r'|}{c}}$$
<div align="right">*Equation 2*</div>

where B is the thermal coefficient of the volume expansion, C_p is the specific heat capacity of the tissue at constant pressure, c is the speed of ultrasound in water set at 1540 m/s, r is the location of the point detector and r' is the location of the absorber as demonstrated in Figure 1 (b). The above equation is used to simulate the point detector with small aperture due to the heat source $H(r, t)$. The equation applies spherical integration with a radius determined by the acoustic time of flight. The constant $B/4\pi C_p$ was set to be 1.

The heating function $H(r, t)$ was computed for individual vessels and generated pressure signals were then superimposed for the entire tree. The model assumes uniform illumination of the laser light with $H(r_{blood}, t) \gg H(r_{tissue}, t)$; in other words, the absorption of blood vessels is significantly larger than the absorption of the surrounding tissues resulting in:

$$H(r,t) = \begin{cases} 1, & \text{in the vessel}, \\ 0, & \text{otherwise}. \end{cases}$$
<div align="right">*Equation 3*</div>

each cylindrical vessel has defined radius, start position and end position specified by the fractal tree geometry.

2.3. Diffusion of blood outside microvessels

To model vascular disruption, the diffusion of extravasated blood outside the vessels was modeled using Fick's Laws [23]. Fick's Law correlates the diffusion flux to the concentration gradient. The rate of change of the concentration at a point in space is proportional to the second derivative of concentration in space with constant diffusion coefficient (d).

The diffused blood (n) at location x and time t for a vessel boundary located at position 0 with initial concentration of n_o was computed using the one-dimension solution to the Fick's Law equation:

$$n\,(x,t) = n_o\,erfc\left(\frac{x}{2\sqrt{d_H t}}\right)$$

Equation 4

where d_H is the diffusion of hemoglobin with a value of 0.0005 mm²/h, erfc is the complementary error function. Cylindrical symmetry was applied to account for the whole vessel. The equation was computed for a single microvessel 10 μm in diameter and 2 mm in length at time intervals $t = 0, 0.1, 0.5,$ and 1.0 hours. This resulted in full width half maxima of the hemoglobin concentration of 10, 24, 40, 52 μm, respectively. These intervals were chosen because preliminary studies from our group suggest that vascular hemorrhaging occurs early after the administration of treatments that target blood vessels [27].
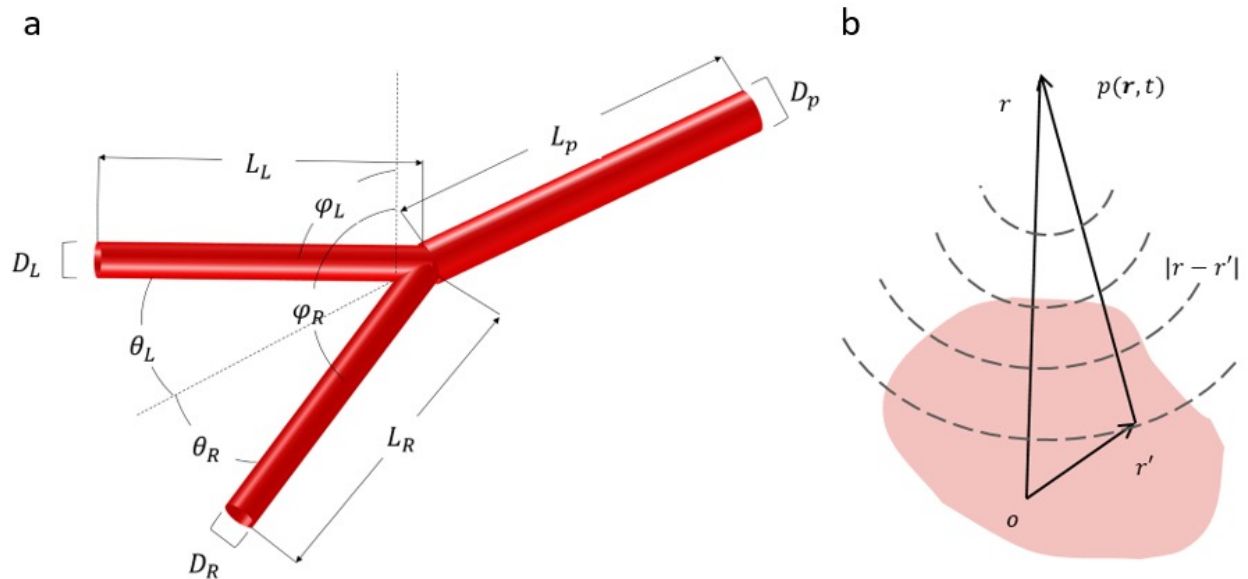
Figure 1: In (a) is an illustration of the fractal tree bases and the parameters for modeling the vascular tree. The parent segment bifurcates into two daughter segments with different diameters and lengths. (b) A schematic representation of the detected photoacoustic signal from an absorber located at r' and a point source located at r.

The concept of diffusion of blood outside the vessels was applied to the vascular tree model. The diffusion of blood was simulated using Fick's Law on vessels smaller than 30 μm in diameter after 0.5 hours of vessel disruption. This was done to account for the effect of a treatment on the microvessels. The generated PA signals of a vascular tree simulated with extravasated blood were compared to a vascular trees without extravasated blood. The comparison includes the generation of B-mode images and spectral analysis of the generated PA signals (Equation 2).

2.4. Signal Simulation and beamforming

The simulated PA signals were generated by taking into account several features of a high frequency commercial ultrasound transducer (Fujifilm-Visual Sonics, Toronto, Canada). It has the capability to image tumours at a depth more than 1 cm with 45 μm lateral spatial resolution. The transducer was simulated for frequency ranges between 15 to 45 MHz (the -6 dB bandwidth) using a Butterworth bandpass filter of order 3 which was applied to the generated PA signals. The PA signals were computed for all 256 elements 14.08 mm in length and 0.055 mm in pitch. The distance of the transducer to the original parent vessel segment was set to be 11 mm which is the approximate focus of the laser beam.

The signals were beamformed using a conventional delay and sum method for every 64 elements. The directivity of the transducer α was accounted for using the equation below:

$$\alpha(\theta) = Re[Jinc(\pi D \lambda^{-1} sin(\theta)]$$

Equation 5

where θ is the angle to the vector line, D is the diameter of a single element in the transducer and λ is the wavelength of the central frequency of the transducer (approximately 50 μm for the speed of sound of 1540 m/s). Finally, apodization of the transducer was applied using a Hamming filter. The generated B-mode images of the vasculature tree with and without extravasated blood were then visually compared.

2.5. Spectral analysis

Spectral analysis was applied to the generated PA signals. The spectral analysis was applied by windowing the simulated PA signals with a Hann window of size 500 μm. The power spectrum of the windowed signals was computed and fitted to a straight line between the ultrasound frequencies of 15 to 45 MHz. The parameters calculated from the fitted line are the spectral slope, MBF and y-intercept. These parameters were compared for parameters derived from the vascular tree with extravasated blood and the vascular tree without extravasated blood.

3.   RESULTS AND DISCUSSION:

3.1. Simulated PA signals of single microvessels

A single microvessel 10 μm in diameter and 2 mm in length was modeled. The PA signal at a point detector 11 mm away from the microvessel source was computed using Equation 2. Hemoglobin diffusion into the interstitium was modeled using Equation 4 to account for microvessel damage due to microbubbles. Spatial and frequency analysis of generated PA signals from the single microvessel are presented in Figure 2. Figure 2 (a) is a schematic representation of the geometry of a simulated microvessel. Figure 2 (b) shows images of the cross-section of two simulated microvessels before vessel disruption and 1 hour after microvessel disruption. This demonstrates the changes in the distribution and content of hemoglobin after bleeding. For bleeding, there is a gradient change in the hemoglobin content once it enters the tissues. In contrast, before bleeding there is a sharp change in the hemoglobin content outside the vessel. This will have an impact in the generated PA signals, as the PA signals are correlated to the spatial distribution of the absorbers.

The effect of a vessel's bleeding on the spatial and frequency content of generated PA signals is presented in Figure 2 (c)-(e). Figure 2 (c) shows the distribution of hemoglobin before (0 hour) and at different time intervals after bleeding (0.1, 0.5 and 1.0 hour). This figure demonstrates the distribution of hemoglobin molecules outside the tissues as time progresses after vessel disruption. Figure 2 (d) shows the simulated PA signals in the spatial domain (time domain multiplied by the speed of sound in water at 37ºC). It can be noted that as time progressed after the vessel damage, the amplitude of the PA signals decreased while the spatial extract of the PA signals increased. The decrease in the amplitude of generated PA signals is due to introducing a gradient change in the hemoglobin content. The spatial span of the PA signals increased with time progression after bleeding due to the extend of hemoglobin to a larger area within the interstitium.

The changes of the PA signals in the spatial domain also produce changes in the power spectra of the signals as shown in Figure 2 (e). Within the bandwidth of 15 – 45 MHz of the transducers we have used in our experiments, the power spectra exhibit significant changes as a result of hemoglobin diffusion into the interstitium [27]. As bleeding progresses, the slope of the power spectra will decrease and the y-intercept will increase. The next step

was to model the PA signals from the entire vascular tree and test if these changes can be detected in the simulated images, and with the proposed spectral techniques.
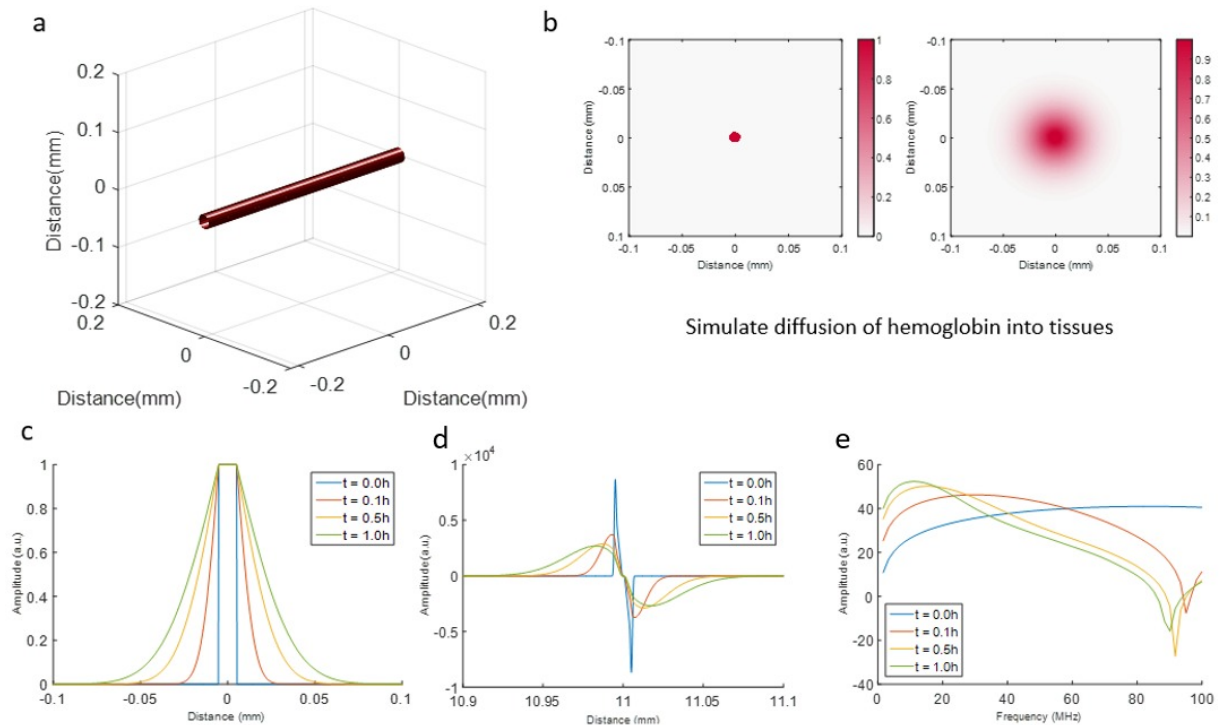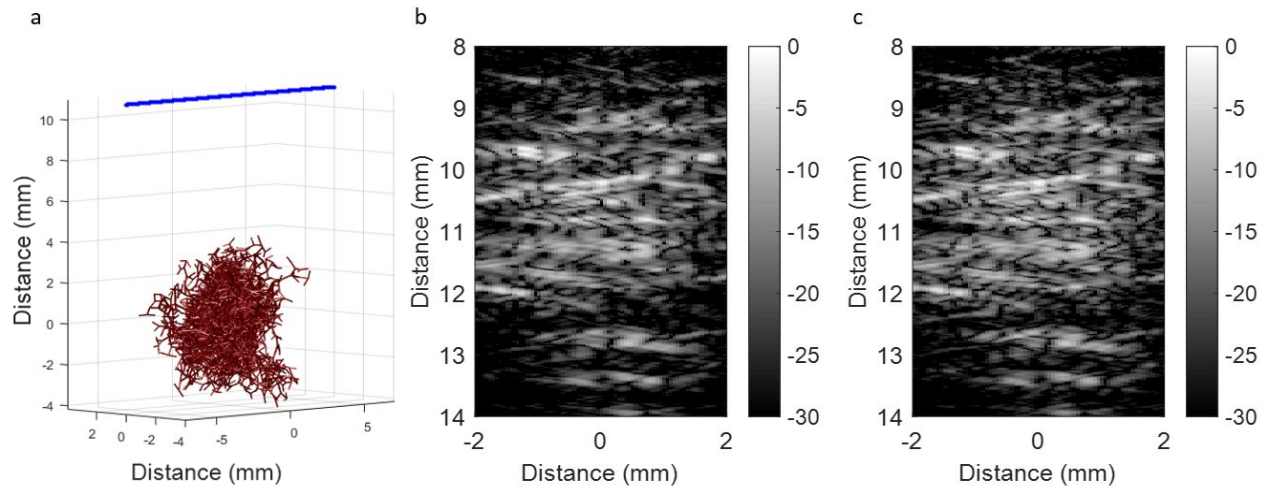

Figure 2: (a) A schematic representation of the simulated vessel geometry. (b) A schematic representation of the cross section of the vessel in (a) before bleeding and after 1 hour of bleeding simulated using Fick's law. (c) Line profile of the blood distribution, generated PA signal in (d) spatial and (e) frequency domains at different time points after vessel disruption.

3.2. Modeling PA signals of vasculature before and after bleeding

An example of simulated tumour vasculatures is presented in Figure 3 (a). It can be noted that the tumour vasculatures are chaotic and dense as it is the case for tumour vasculatures [28]. The location of the transducer is denoted by the blue dots for 256 elements. The beamformed images for the selected bandwidth of 15 – 45 MHz are presented in Figure 3 (b) and (c) for vascular trees without bleeding and 0.5 hour after bleeding. The results in Figure 3 demonstrate the challenge of detecting the bleeding from non-resolvable microvessels in ultrasound resolved PA imaging as the size of the vessels are smaller than the system resolution of 50 µm. Visual inspection of the B-mode images illustrates that it is hard to distinguish between the images generated from the bleeding and non-bleeding vessels.

Spatial and frequency domain signals of simulated PA signals generated from the vascular tree model are presented in Figure 4. The time-domain PA signals simulated before bleeding and 0.5 hours after bleeding are shown in (a) for non band-limited signals and (b) band-limited signals. Again, it is difficult to distinguish between the two cases by visual inspection of the PA signals. Figure 4 (c) presents the average power spectra (of 256 elements for four different trees) and the line best fitted before bleeding and 0.5 hour after bleeding. The line fitted to the power spectra demonstrates a change between the two groups and these changes are more pronounced at higher frequencies.

Figure 3: (a) A schematic representation of the simulated vascular tree. The blue dots represent the location of the simulated point source detector. (b) and (c) The beamformed image of the vascular tree in (a) without microvessels bleeding and 0.5 hour after microvessels bleeding respectively.
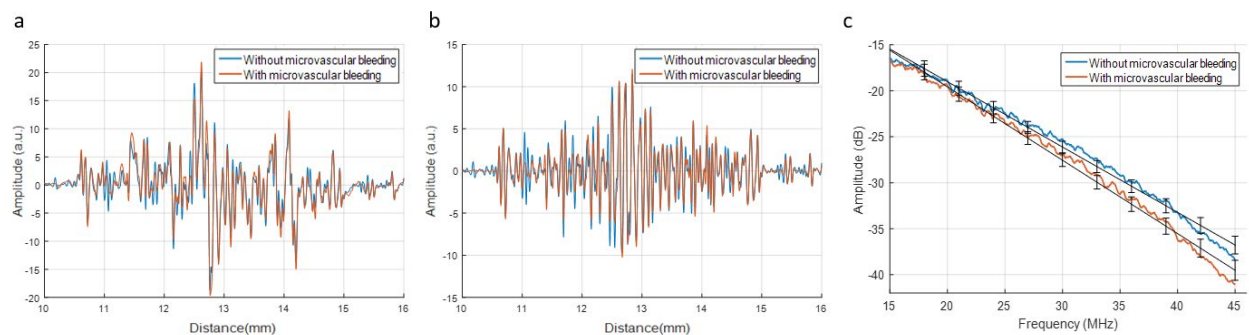

Figure 4: Representative PA signals acquired from simulating vascular tree without microvessel bleeding and 0.5 hours after microvessels bleeding of non band-limited (a) and band-limited signals (15 – 45 MHz) (d). (c) The average power spectra of four different vascular trees and the average line best fitted with its standard deviation.

Comparison of the selected spectral analysis parameters between three simulated groups are presented in Figure 5. These three groups represent the analysis of PA signals done before bleeding, 0.5 hour after bleeding and 1 hour after bleeding. The spectral slope is presented to the left of Figure 5, the slope decreasing significantly as early as 0.5 hour of bleeding ($p < 0.01$). The spectral slope is correlated to the size of the source [8], [11], [29], [30]. A decrease in the spectral slope at these frequencies correlates to an increase in the size of the PA source. This is due to the diffusion of hemoglobin into the interstitium that generates an overall larger PA source. The decrease in spectral slope following vessel destruction has been observed experimentally [27]. The middle bar plotted in Figure 5 compares the y-intercept parameter; the y-intercept parameter is correlated to the concentration of the optical absorbers [8], [29], [30]. The decrease in the y-intercept parameter as bleeding progressed. However, these changes are not significant when modeling an entire vascular tree. To the right of Figure 5 is the MBF, which is a dependent parameter that combines the effect of the spectral slope and y-intercept. The results demonstrate a significant decrease in the MBF parameter 0.5 hour after bleeding ($p < 0.01$).

Spectral analysis of simulated PA signals could be used to differentiated between vasculatures before bleeding and 0.5 hours after bleeding through analysis of the changes in the spectral slope. The decrease in the spectral slope

could be correlated to the effective increase of the microvessels size after bleeding occurs. The MBF could also be used to detect microvessel bleeding, and it is an independent variable to the spectral slope.

The study introduces the technique of detecting vessel bleeding based on spectral parameters of PA signals. There may be other changes that can be detected, which can be confirmed by further simulations, which can be done to account for the distribution of multiple chromophores. For example as red blood cells escape the vessels, the concentration of deoxyhemoglobin and methemoglobin rises due to changes in the surrounding environment the [23], [31]. These changes will result in different PA signals at different optical wavelengths. The chromophores distribution as a result of bleeding can be modeled using the vascular tree and its effect on generated PA signals can be tested for different wavelengths. Finally, the simulations can be compared to experimental results of tumour mouse model treated with microbubbles.
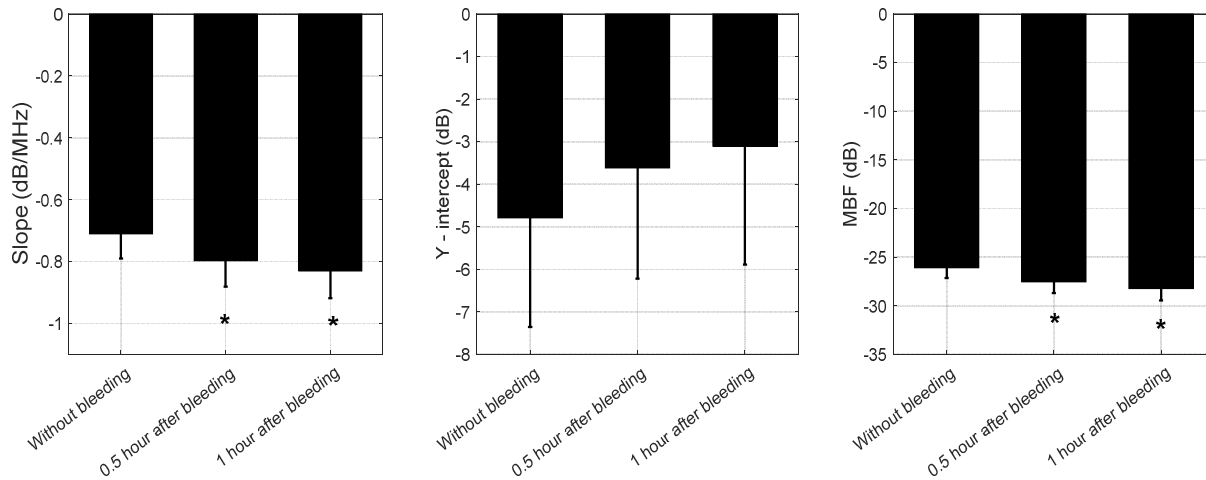
Figure 5: Spectral parameters acquired from vascular tree model simulation. The calculated parameters are the slope, y-intercept and MBF for the three groups of simulated vascular trees to represent an intact tumour vasculature, 0.5 hour after bleeding and 1 hour after bleeding. *: A star indicates statistical significance compared to the without bleeding group.

4. CONCLUSION

This study demonstrates the capability of PA spectral analysis in detecting structural changes due to bleeding at the micron scale. According to the simulations performed, microvessel bleeding can be detected by quantifying changes in the spectral slope and MBF of the power spectra in ultrasound resolution PA. This demonstrates a potential for the use of PA spectral analysis for cancer treatment monitoring, and for treatments that target the vasculature. The early clinical feedback that could be potentially obtained by detection and quantification of microvessel bleeding may result in a significant improvement in treatment outcome. It may also result in a reduction in the reoccurrence rate of tumours through feedback provided on the efficacy of the treatment, and through using bleeding as a biomarker of tumour response.

5. ACKNOWLEDGMENTS

6. REFERENCES

[1] S. Mallidi, K. Watanabe, D. Timerman, D. Schoenfeld, and T. Hasan, "Prediction of Tumor Recurrence and Therapy Monitoring Using Ultrasound-Guided Photoacoustic Imaging," *Theranostics*, vol. 5, no. 3, pp. 289–301, Jan. 2015.

[2] K. Briggs, A. Al Mahrouki, J. Nofiele, A. El-Falou, M. Stanisz, H. C. Kim, M. C. Kolios, and G. J. Czarnota, "Non-invasive monitoring of ultrasound-stimulated microbubble radiation enhancement using photoacoustic imaging," *Technol. Cancer Res. Treat.*, vol. 13, no. 5, pp. 435–444, Oct. 2014.

[3] G. J. Czarnota, R. Karshafian, P. N. Burns, S. Wong, A. A. Mahrouki, J. W. Lee, A. Caissie, W. Tran, C. Kim, M. Furukawa, E. Wong, and A. Giles, "Tumor radiation response enhancement by acoustical stimulation of the vasculature," *Proc. Natl. Acad. Sci.*, vol. 109, no. 30, pp. E2033–E2041, Jul. 2012.

[4] D. L. Miller and J. Quddus, "Diagnostic ultrasound activation of contrast agent gas bodies induces capillary rupture in mice," *Proc. Natl. Acad. Sci. U. S. A.*, vol. 97, no. 18, pp. 10179–10184, 2000.

[5] N. Kobayashi, T. Yasu, S. Yamada, N. Kudo, M. Kuroki, M. Kawakami, K. Miyatake, and M. Saito, "Endothelial cell injury in venule and capillary induced by contrast ultrasonography," *Ultrasound Med. Biol.*, vol. 28, no. 7, pp. 949–956, Jul. 2002.

[6] D. M. Skyba, R. J. Price, A. Z. Linka, T. C. Skalak, and S. Kaul, "Direct in vivo visualization of intravascular destruction of microbubbles by ultrasound and its local effects on tissue," *Circulation*, vol. 98, no. 4, pp. 290–293, Jul. 1998.

[7] L. V. Wang and S. Hu, "Photoacoustic Tomography: In Vivo Imaging from Organelles to Organs," *Science*, vol. 335, no. 6075, pp. 1458–1462, Mar. 2012.

[8] F. L. Lizzi, M. Greenebaum, E. J. Feleppa, M. Elbaum, and D. J. Coleman, "Theoretical framework for spectrum analysis in ultrasonic tissue characterization," *J. Acoust. Soc. Am.*, vol. 73, no. 4, pp. 1366–1373, Apr. 1983.

[9] J. Mamou and M. L. Oelze, Eds., *Quantitative ultrasound in soft tissues*. Dordrecht: Springer, 2013.

[10] Y. Yang, S. Wang, C. Tao, X. Wang, and X. Liu, "Photoacoustic tomography of tissue subwavelength microstructure with a narrowband and low frequency system," *Appl. Phys. Lett.*, vol. 101, no. 3, p. 034105, Jul. 2012.

[11] G. Xu, I. A. Dar, C. Tao, X. Liu, C. X. Deng, and X. Wang, "Photoacoustic spectrum analysis for microstructure characterization in biological tissue: A feasibility study," *Appl. Phys. Lett.*, vol. 101, no. 22, p. 221102, Nov. 2012.

[12] T. Feng, J. E. Perosky, K. M. Kozloff, G. Xu, Q. Cheng, S. Du, J. Yuan, C. X. Deng, and X. Wang, "Characterization of bone microstructure using photoacoustic spectrum analysis," *Opt. Express*, vol. 23, no. 19, p. 25217, Sep. 2015.

[13] R. E. Kumon, C. X. Deng, and X. Wang, "Frequency-domain analysis of photoacoustic imaging data from prostate adenocarcinoma tumors in a murine model," *Ultrasound Med. Biol.*, vol. 37, no. 5, pp. 834–839, May 2011.

[14] G. Xu, Z.-X. Meng, J. D. Lin, J. Yuan, P. L. Carson, B. Joshi, and X. Wang, "The Functional Pitch of an Organ: Quantification of Tissue Texture with Photoacoustic Spectrum Analysis," *Radiology*, vol. 271, no. 1, pp. 248–254, Apr. 2014.

[15] E. Hysi, R. K. Saha, and M. C. Kolios, "Photoacoustic ultrasound spectroscopy for assessing red blood cell aggregation and oxygenation," *J. Biomed. Opt.*, vol. 17, no. 12, p. 125006, Dec. 2012.

[16] E. M. Strohm, E. S. L. Berndl, and M. C. Kolios, "Probing Red Blood Cell Morphology Using High-Frequency Photoacoustics," *Biophys. J.*, vol. 105, no. 1, pp. 59–67, Jul. 2013.

[17] E. M. Strohm, I. Gorelikov, N. Matsuura, and M. C. Kolios, "Modeling photoacoustic spectral features of micron-sized particles," *Phys. Med. Biol.*, vol. 59, no. 19, pp. 5795–5810, Oct. 2014.

[18] R. Karshafian, P. N. Burns, and M. R. Henkelman, "Transit time kinetics in ordered and disordered vascular trees," *Phys. Med. Biol.*, vol. 48, no. 19, pp. 3225–3237, Oct. 2003.

[19] J. Zalev, "Detection and monitoring for cancer and abnormal vasculature by photoacoustic signal characterization of structural morphology." .

[20] M. N. Fadhel and M. C. Kolios, "Photoacoustic speckle and spectral analysis of vasculature trees," presented at the IFMBE Proceedings, 2015, vol. 51, pp. 1084–1087.

[21] J. Zalev and M. C. Kolios, "Detecting abnormal vasculature from photoacoustic signals using wavelet-packet features," presented at the Progress in Biomedical Optics and Imaging - Proceedings of SPIE, 2011, vol. 7899.

[22] B. Pourebrahimi, A. Al-Mahrouki, J. Zalev, J. Nofiele, G. J. Czarnota, and M. C. Kolios, "Classifying normal and abnormal vascular tissues using photoacoustic signals," presented at the Progress in Biomedical Optics and Imaging - Proceedings of SPIE, 2013, vol. 8581.

[23] L. L. Randeberg, O. A. Haugen, R. Haaverstad, and L. O. Svaasand, "A novel approach to age determination of traumatic injuries by reflectance spectroscopy," *Lasers Surg. Med.*, vol. 38, no. 4, pp. 277–289, Apr. 2006.

[24] L. Vidovič, M. Milanič, and B. Majaron, "Assessment of hemoglobin dynamics in traumatic bruises using temperature depth profiling," presented at the Society of Photo-Optical Instrumentation Engineers (SPIE) Conference Series, 2013, vol. 9032, p. 903202.

[25] P. Naglič, L. Vidovič, M. Milanič, L. L. Randeberg, and B. Majaron, "Applicability of diffusion approximation in analysis of diffuse reflectance spectra from healthy human skin," 2013, vol. 9032, p. 90320N–90320N–12.

[26] J. R. Less, T. C. Skalak, E. M. Sevick, and R. K. Jain, "Microvascular architecture in a mammary carcinoma: branching patterns and vessel dimensions," *Cancer Res.*, vol. 51, no. 1, pp. 265–273, Jan. 1991.

[27] E. Hysi, J. P. May, L. Writzfeld, E. Undyzs, S.-D. Li, and M. C. Kolios, "Probing the in vivo changes in oxygen saturation with photoacoustic imaging as a non-invasive means of assessing treatment progression," presented at the Progress in Biomedical Optics and Imaging - Proceedings of SPIE, 2015, vol. 9323.

[28] N. Weidner, J. P. Semple, W. R. Welch, and J. Folkman, "Tumor Angiogenesis and Metastasis — Correlation in Invasive Breast Carcinoma," *N. Engl. J. Med.*, vol. 324, no. 1, pp. 1–8, Jan. 1991.

[29] M. L. Oelze, J. F. Zachary, and W. D. O'Brien, "Characterization of tissue microstructure using ultrasonic backscatter: theory and technique for optimization using a Gaussian form factor," *J. Acoust. Soc. Am.*, vol. 112, no. 3 Pt 1, pp. 1202–1211, Sep. 2002.

[30] J. Mamou, A. Coron, M. Hata, J. Machi, E. Yanagihara, P. Laugier, and E. J. Feleppa, "Three-dimensional High-frequency Characterization of Cancerous Lymph Nodes," *Ultrasound Med. Biol.*, vol. 36, no. 3, pp. 361–375, Mar. 2010.

[31] J. Umbreit, "Methemoglobin--it's not just blue: a concise review," *Am. J. Hematol.*, vol. 82, no. 2, pp. 134–144, Feb. 2007.